Table of Contents

Table S1. Crystallographic data and structure refinements for **1-3**

	Ce-fdh (**1**)	Pr-fdh (**2**)	Nd-fdh (**3**)
Molecular formula	$C_{34}H_{38}O_6N_2F_9Ce$	$C_{34}H_{38}O_6N_2F_9Pr$	$C_{34}H_{38}O_6N_2F_9Nd$
Mr	881.77	882.57	885.91
Crystal system	triclinic	Triclinic	Triclinic
Space group	$P\bar{1}$	$P\bar{1}$	$P\bar{1}$
a, Å	9.5494(3)	9.5517(3)	9.5480(4)
b, Å	12.2844(6)	12.2277(4)	12.2023(5)
c, Å	17.9636(5)	17.9577(5)	17.9158(7)
α, °	99.984(3)	99.871(2)	99.810(3)
β, °	104.048(3)	103.967(3)	103.867(3)
γ, °	101.288(3)	101.416(3)	101.481(3)
V, Å^3	1949.93	1941.4	1933.07
Z	2	2	2
T, K	180	180	180
F(000)	886	888	890
λ, Å	0.71073	0.71073	0.71073
$R_1(I \geq 2\sigma(I))$	0.0433	0.0336	0.0453
wR_2(all data)	0.0921	0. 0751	0.0947
S	1.052	1.060	1.070

Table S2. Selected bond lengths (Å) and angles (°) of **1-3**

	Ce-fdh (**1**)	Pr-fdh (**2**)	Nd-fdh (**3**)
Ln-O(1)	2.426(2)	2.410(2)	2.395(3)
Ln-O(2)	2.433(2)	2.415(2)	2.402(3)
Ln-O(3)	2.436(3)	2.409(2)	2.395(3)
Ln-O(4)	2.460(3)	2.442(2)	2.429(3)
Ln-O(5)	2.422(3)	2.400(2)	2.384(3)
Ln-O(6)	2.437(3)	2.416(2)	2.403(3)
Ln-N(1)	2.655(3)	2.631(3)	2.609(4)
Ln-N(2)	2.696(3)	2.670(3)	2.652(4)
O(1)- Ln-O(2)	70.08(8)	70.73(8)	71.08(10)
O(1)- Ln-O(4)	74.75(8)	75.06(8)	75.03(10)
O(1)- Ln-O(6)	123.19(9)	122.43(8)	122.86(10)
O(1)- Ln-N(1)	147.06(9)	147.60(8)	147.62(12)
O(1)- Ln-N(2)	145.17(9)	144.53(8)	144.14(11)
O(2)- Ln-O(4)	133.86(8)	134.72(8)	135.25(10)
O(2)- Ln-O(6)	76.47(8)	75.72(8)	75.52(10)
O(2)- Ln-N(1)	87.72(8)	87.38(8)	87.26(11)
O(2)- Ln-N(2)	144.74(9)	144.74(8)	144.78(11)
O(3)- Ln-O(1)	80.80(9)	81.43(8)	81.36(11)
O(3)- Ln-O(2)	76.15(8)	76.32(8)	76.29(10)
O(3)- Ln-O(4)	69.48(8)	69.96(7)	70.42(10)

O(3)- Ln-O(6)	133.15(8)	133.10(8)	132.73(11)
O(3)- Ln-N(1)	70.16(9)	70.08(8)	70.04(11)
O(3)- Ln-N(2)	103.59(9)	103.96(8)	104.19(11)
O(4)- Ln-N(1)	107.73(9)	107.77(8)	107.80(10)
O(4)- Ln-N(2)	74.71(8)	74.19(8)	73.81(10)
O(5)- Ln-O(1)	86.94(8)	85.35(8)	84.97(11)
O(5)- Ln-O(2)	117.27(8)	116.60(7)	116.49(10)
O(5)- Ln-O(3)	157.44(9)	157.14(8)	156.95(10)
O(5)- Ln-O(4)	89.10(8)	88.67(8)	88.18(10)
O(5)- Ln-O(6)	69.34(8)	69.75(8)	70.31(10)
O(5)- Ln-N(1)	125.52(9)	126.51(8)	126.91(11)
O(5)- Ln-N(2)	76.24(8)	76.71(8)	76.77(11)
O(6)- Ln-O(4)	149.47(8)	149.33(8)	149.02(10)
O(6)- Ln-N(1)	71.47(9)	71.75(8)	71.46(11)
O(6)- Ln-N(2)	79.18(9)	79.64(8)	79.57(10)
N(1)- Ln-N(2)	60.35(9)	60.90(8)	61.16(12)

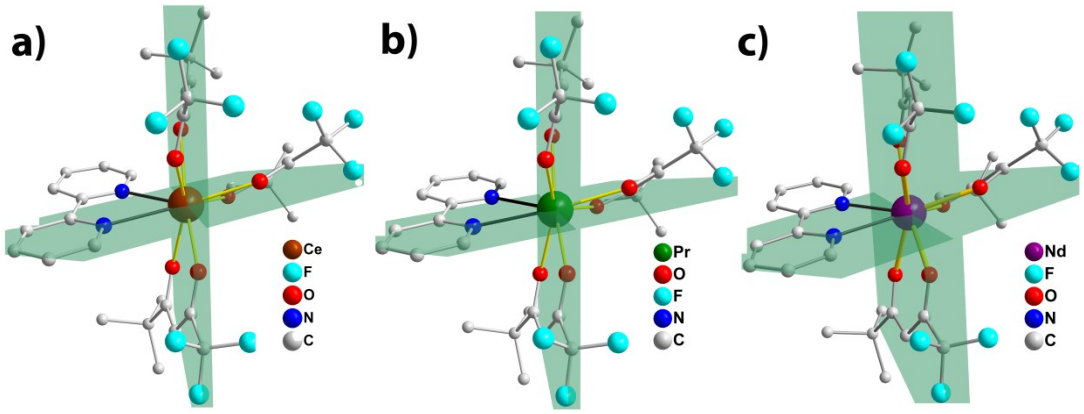

Figure S1. View of molecular structures of **1-3**. The green planes represent the planes described in the main text.

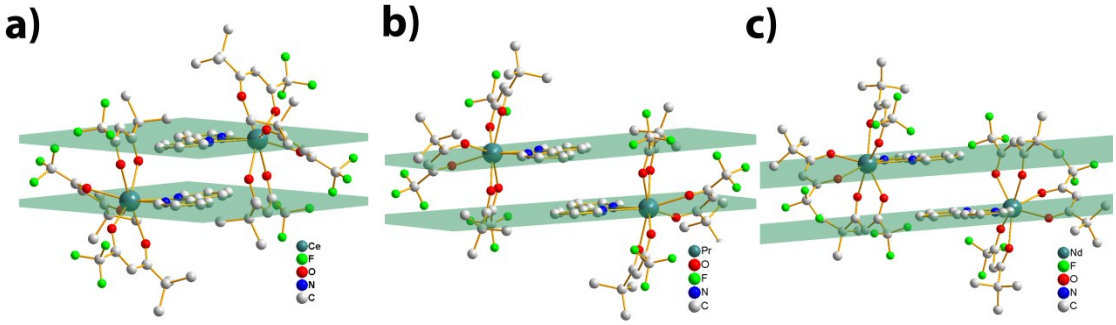

Figure S2. View of π-π stacking in **1-3**. The green planes represent the bpy planes described in the main text.

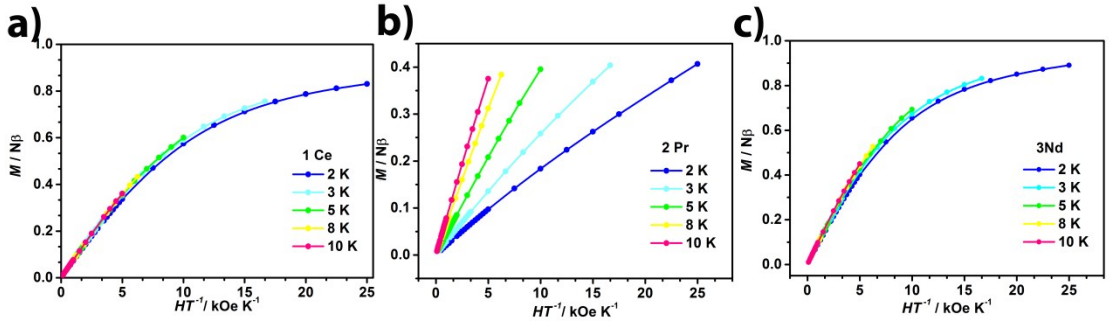

Figure S3. *M* versus *H/T* plots for **1-3**

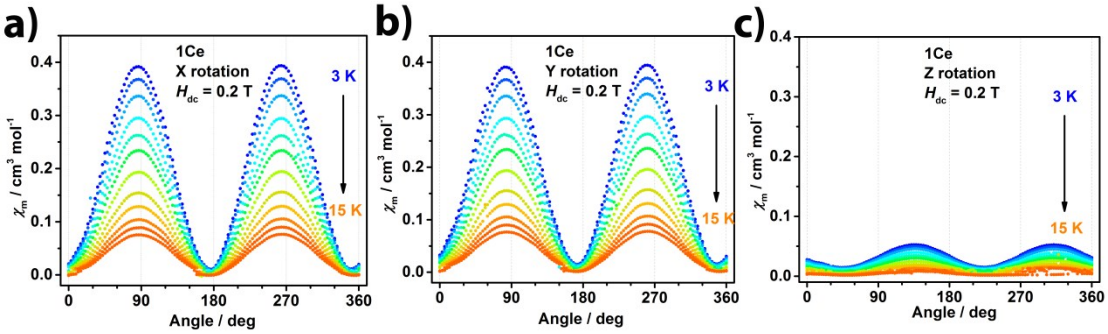

Figure S4. Angular dependence of magnetic susceptibility along XYZ rotation for **1**

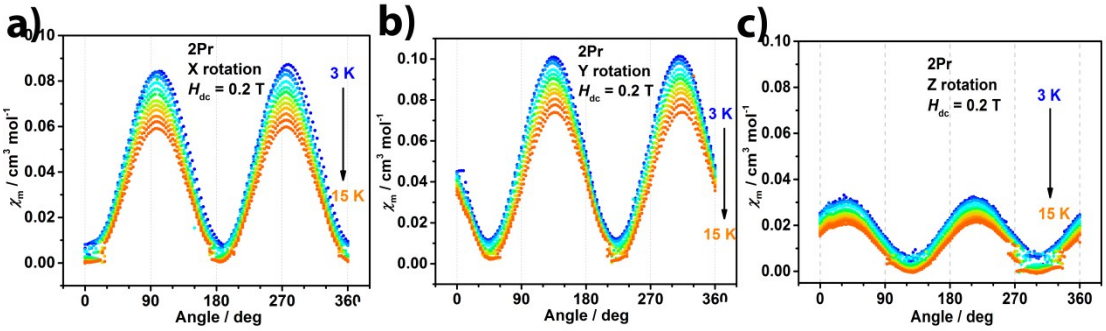

Figure S5. Angular dependence of magnetic susceptibility along XYZ rotation for **2**

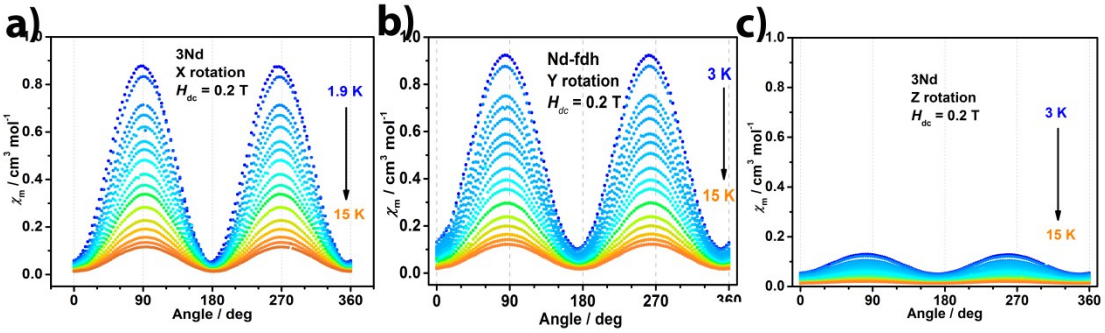

Figure S6. Angular dependence of magnetic susceptibility along XYZ rotation for **3**

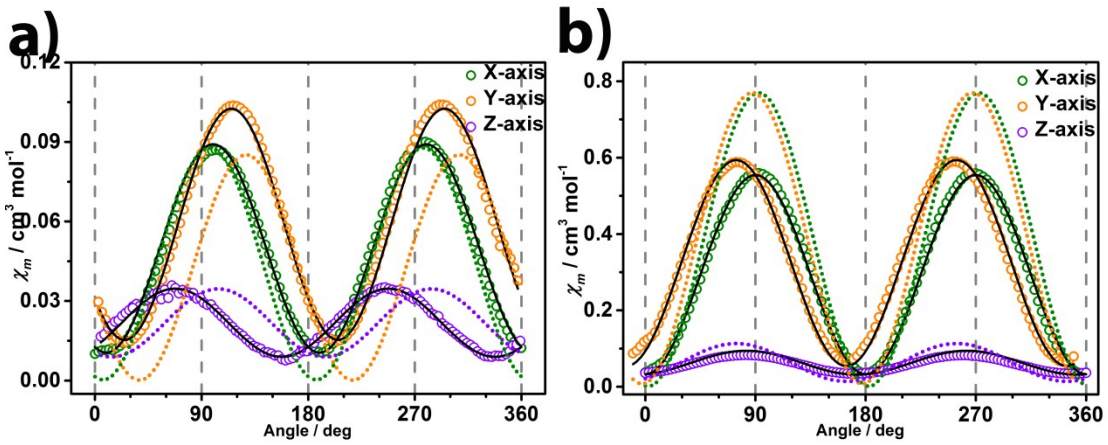

Figure S7. Angular dependence of susceptibility at 3 K under 2 kOe for a)Pr and b)Nd. Experimental (circles), fitting (solid) and *ab initio* calculation (dashed).

Table S3. Values ($cm^3 \cdot K \cdot mol^{-1}$) of corresponding principal axis of **1-3**

	1 Ce^{III}			**2 Pr^{III}**			**3 Nd^{III}**		
T **/ K**	χ_{zz}	χ_{xx}	χ_{yy}	χ_{zz}	χ_{xx}	χ_{yy}	χ_{zz}	χ_{xx}	χ_{yy}
3.0	0.4020	0.0254	0.0122	0.1052	0.0164	0.0089	0.58299	0.05969	0.02852
3.2	0.3770	0.0254	0.0122	0.1026	0.0181	0.0072	0.54616	0.05717	0.02673
3.5	0.3450	0.0241	0.0111	0.1008	0.0173	0.0068	0.49895	0.05278	0.0258
4.0	0.3016	0.0228	0.0102	0.0978	0.0159	0.0053	0.43655	0.04638	0.02188
4.5	0.2684	0.0188	0.0085	0.0954	0.0145	0.0038	0.38961	0.04067	0.01901
5.0	0.2400	0.0164	0.0063	0.0937	0.013	0.0029	0.3489	0.03636	0.01738
6.0	0.1994	0.0137	0.0056	0.0911	0.0119	0.0025	0.29067	0.03038	0.01471
7.5	0.1599	0.0112	0.0037	0.089	0.0113	0.0012	0.23261	0.02441	0.01228
9.0	0.1335	0.0096	0.0024	0.0869	0.0101	0.0012	0.1941	0.02048	0.01047
11.0	0.1086	0.0076	0.0015	0.084	0.0096	0.0006	0.15891	0.01667	0.00889
12.8	0.0929	0.0061	0.0007	0.0813	0.0088	0.0005	0.13608	0.01431	0.00782
15.0	0.0791	0.0040	0.0006	0.0776	0.0083	0.0004	0.11626	0.01286	0.00683

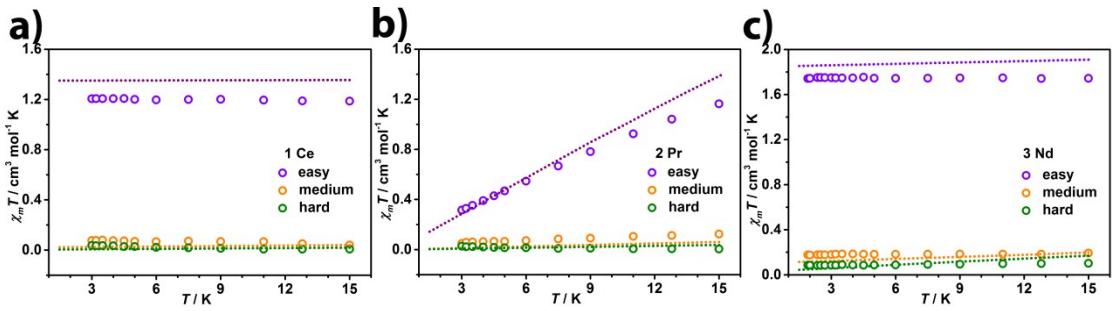

Figure S8. Comparison of the $\chi_m T$ values along easy/medium/hard axes of **1-3** from experiments (circle) and *ab initio* calculations

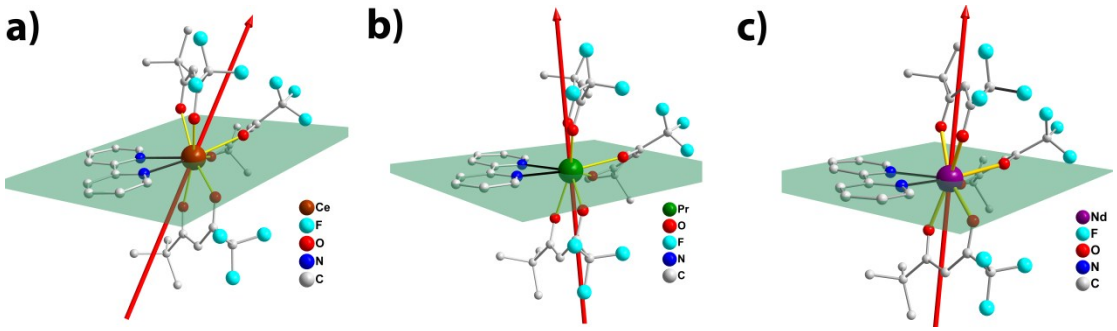

Figure S9. Easy axis (red) direction of **1-3;** The green plane represents the bpy plane as described in the main text.

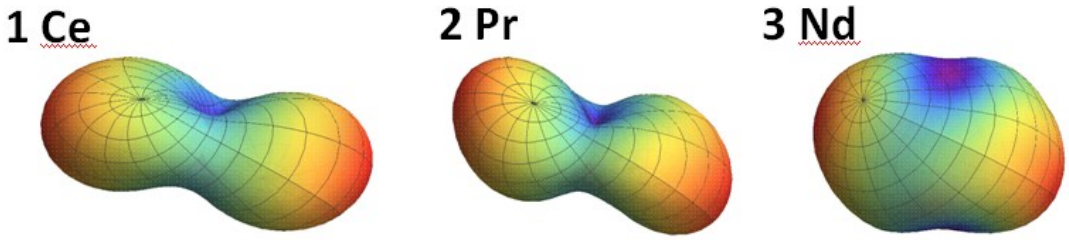

Figure S10. Electrostatic potential surface of Ising ground states. From left to right represented | ±5/2 > for Ce^{III} , | ±4 > for Pr^{III}, and | ±9/2 > for Nd^{III}.

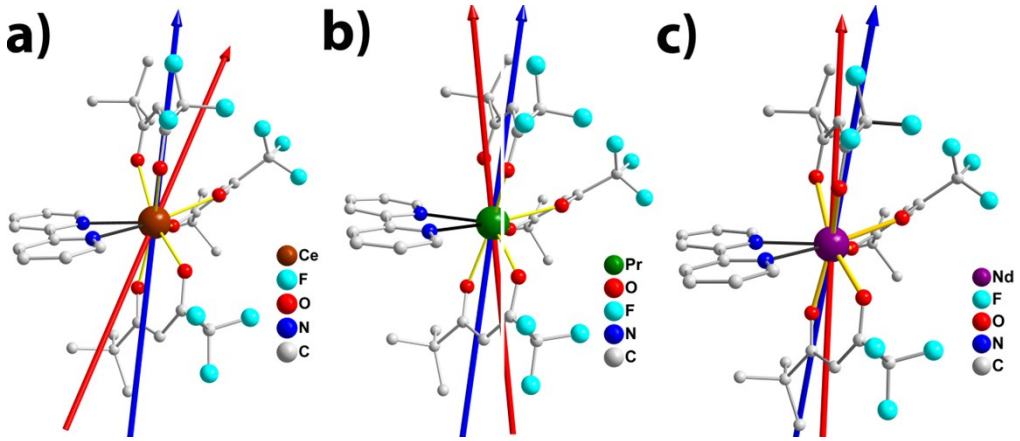

Figure S11. The red and blue arrows indicate the magnetic easy axis directions of **1-3** determined from experiments and electrostatic simulations, respectively.

Table S4. Energy levles determined by *an initio* for **1-3**

Energy State (cm^{-1})	**1Ce^{III}**	**2Pr^{III}**	**3Nd^{III}**
1	0	0	0
2	0	45.10	0
3	339.63	234.41	106.42
4	339.63	330.21	106.42
5	685.46	453.23	166.40
6	685.46	582.04	166.40
7		628.24	268.87
8		789.06	268.87
9		830.86	408.62
10			408.62

Table S5. *g* tensors of the ground state for **1-3**

	1Ce^{III}		**3Nd^{III}**	
	Ab initio	Exp	Ab initio	Exp
g_x	0.176	0.28	0.56	1.04
g_y	0.46	0.66	1.06	1.43
g_z	3.79	3.56	4.78	4.31

Table S6. Wave function composition of two low-lying states for **1-3** calcualted by *ab initio*

1Ce^{III}			**2Pr^{III}**			**3Nd^{III}**		
Wave function Composition of ground state								
M_J	**Ground doublet**		M_J	**State1**	**State2**	M_J	**Ground doublet**	
-5/2	25.38%	66.57%	**-4**	36.12%	44.03%	**-9/2**	62.27%	0.25%
-3/2	1.22%	0.21%	**-3**	1.51%	1.99%	**-7/2**	0.21%	0.52%
-1/2	3.38%	3.25%	**-2**	8.07%	3.56%	**-5/2**	12.14%	0.95%
+1/2	3.25%	3.38%	**-1**	2.11%	0.23%	**-3/2**	12.47%	0.56%

+3/2	0.21%	1.22%	**0**	4.38%	0.40%	**-1/2**	8.99%	1.64%
+5/2	66.57%	25.38%	**1**	2.11%	0.23%	**+1/2**	1.64%	8.99%
			2	8.07%	3.56%	**+3/2**	0.56%	12.47%
			3	1.51%	1.99%	**+5/2**	0.95%	12.14%
			4	36.12%	44.03%	**+7/2**	0.52%	0.21%
						+9/2	0.25%	62.27%

Composition of Ground states calculated by *ab initio*

Ce^{III}: 0.92 | ±5/2 > + 0.014 | ±3/2 > + 0.066 | ±1/2 >

Pr^{III}: 0.72 | ±4 > + 0.03 | ±3 > + 0.16 | ±2 > + 0.04 | ±1 > + 0.05 | 0 >

Nd^{III}: 0.62 | ±9/2 > + 0.01 | ±7/2 > + 0.13 | ±5/2 > + 0.13 | ±3/2 > + 0.11 | ±1/2 >

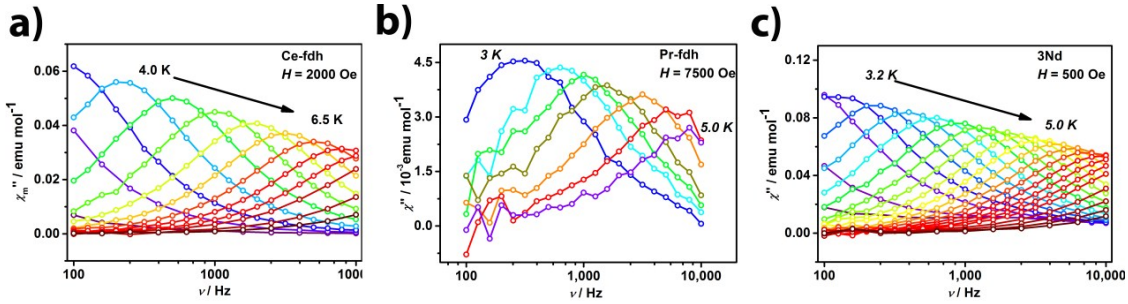

Figure S12. Out-of-phase signal (χ_m'') versus frequency (ν) plots for **1-3**.

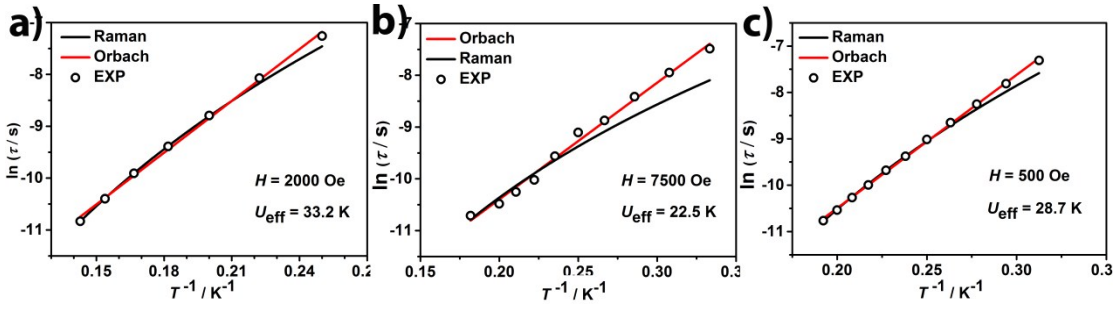

Figure S13. Relaxation time (lnτ) versus inverse of temperature (T^{-1}) plots for **1Ce**(a), **2Pr**(b) and **3Nd**(c). The solid lines represent the fitting Orbach process (red) by $\tau^{-1}=\tau_0\exp(-U_{eff}/T)$, and Raman process (black) by $\tau^{-1}=CT^n$.

Discussion：

The effective energy barriers are as shown in table below by fitting lnτ vs 1/T using a linear Orbach process, but much smaller than the theoretical ones depicted in the main text. Raman process fitting plots for **1** and **3** feature as identically as Orbach plot in the studied temperature and frequency range, with parameter n in the common range of 4~9. However, it may be more complicated for **2** with over-large standard error for parameter C and smaller R^2 probably due to the non-Kramers nature of Pr^{III}. Considering the much smaller U_{eff} than theoretical energy levels, we may prefer a Raman process dominated relaxation in **1** and **3**. However, seriously speaking, due to insufficient experimental data points and *ab initio* calculation errors, we must take into account the inaccuracy of the results above.

Table S7. Detailed parameters fit by Orbach and Raman process for **1-3**

	Orbach $\tau^{-1}=\tau_0\times\exp(-U_{eff}/T)$					**Raman** $\tau^{-1}=C\times T^{\wedge n}$				
	τ_0 / s^{-1}	*St.E.*τ_0	U_{eff} / K	*St.E.*U_{eff}	R^2	C	*St.E.C*	n	*St.E.n*	R^2
1Ce	1.8E-7	0.14	33.3	0.74	0.997	0.40	0.05	6.0	0.07	0.999
2Pr	3.3E-7	0.17	22.5	0.69	0.991	25.1	15.0	4.4	0.36	0.963
3Nd	9.2E-8	0.07	28.8	0.28	0.999	0.93	0.12	6.6	0.08	0.999

(*St.E.* abbreviated for Standard Error)